Crustal structures inferred from Bouguer gravity anomalies in the Altai Orogen, Junggar Basin, Tianshan Orogen, and Tarim Basin

Xiaosan Zhu [*], Yusen Huang, Tao Wang, He Huang, Hongwei Zheng

Institute of Geology, Chinese Academy of Geological Sciences, Beijing 100037, PR China

ABSTRACT

Based on a Bouguer gravity dataset, we investigate the crustal structures in the region across the Chinese Altai Orogen, Junggar Basin, Tianshan Orogen, and Tarim Basin. Combined with magnetic anomalies and crustal thickness data, the Bouguer gravity anomalies are used to identify regional faults and to infer the basement composition in the Junggar Basin. The regional fault distribution shows that multiple tectonic detachment surfaces may exist in the crust and upper mantle of the Chinese Altai Orogen. The mountain roots mentioned in previous studies may not exist in the Tianshan Orogen, where lower-crustal materials have likely been incorporated into the uppermost mantle. The Tarim Basin consists of Archaean-Palaeoproterozoic crystalline basement and Meso-Neoproterozoic metamorphic basement with high Bouguer gravity anomalies. The tectonic sutures can be inferred from the lateral variation of the Bouguer gravity and improve our understanding of the evolution of the southwestern Central Asian Orogenic Belt.

1. Introduction

The Central Asian Orogenic Belt (CAOB) (e.g., Jahn et al., 2000; Windley et al., 2007), including the Altaids (Şengör and Natal'in, 1996; Şengör et al., 2022) and Urbaykalides around the periphery of the Siberian and Eastern European cratons, is a giant orogenic collage located between the Eastern European (Baltic), Siberian, Tarim, and North China cratons (Fig. 1) (Xiao et al., 2008, 2009, 2018, 2019; Xiao and Santosh, 2014). The CAOB extends from the Caspian Sea in the west to the border of the northwestern Pacific Ocean in the east, spanning Russia, Kazakhstan, Kyrgyzstan, Uzbekistan, Tajikistan, Mongolia, and northern China (Xiao and Santosh, 2014). The CAOB is the world's largest accretionary orogenic belt and has the longest geological history and most complex geological structure (Windley et al., 1990, 2007; Xiao et al., 2008, 2009, 2015a, 2015b, 2019; Gao et al., 2018).

Numerous studies have been conducted on the lithospheric structures and compositions of accretionary complexes in the CAOB using geophysical (e.g., Gao et al., 2002; Jiang et al., 2016; Xu et al., 2016; Zheng et al., 2021), geochemical (de Jong, 2009; Geng et al., 2009; Long et al., 2010a; Xiao and Santosh, 2014; Jiang et al., 2016; Chen et al., 2017; Wang et al., 2023a, 2023b), and geological (Li, 1985, 1986; Şengör and Natal'in, 1996; Xiao et al., 2010; Li et al., 2019) information. Geophysical investigations of the CAOB have included analysis of the seismic velocity (Gao et al., 2002; Wang et al., 2004, 2020; Li et al., 2006, 2019; Wu et al., 2018; Yang et al., 2022), density (Wang et al., 2004; Zhao et al., 2004; Jiang et al., 2016; Guy et al., 2020), magnetic susceptibility (Zheng et al., 2021; Zhu et al., 2022a), and resistivity (Yang et al., 2015a, 2015b; Xu et al., 2016). These previous studies have revealed that the Altai Mountains, Junggar Basin, Tianshan Mountains, and Tarim Basin are ideal locations for gaining insights into the tectonic framework and geological evolution of the CAOB.

Various studies have provided information about the crustal structures of the Chinese Altai Mountains (Zhao et al., 2004; Xu et al., 2016), the Junggar region (Jiang, 1984; Wu et al., 2018; Guy et al., 2020; Zhang et al., 2021), and the Tarim Basin (Zhao et al., 2004; Yang et al., 2015a, 2015b), as well as the crustal and upper-mantle structures of the Tianshan Mountains (Gao et al., 2001; Zhao et al., 2004; Li et al., 2006; Li et al., 2019). In particular, information has been obtained about the nature of the basement of the Junggar Basin, which has been proposed to be composed of either Precambrian crystalline rocks (Ren, 1984; Wang, 1986; Wu, 1986) or Palaeozoic oceanic crustal material (Coleman, 1989; Feng et al., 1989; Xu et al., 2020; Zhu et al., 2022a). However, a full geophysical characterisation of the crustal structure of these regions is required and the nature of the basement in the Junggar Basin remains uncertain.

In this study, we processed and inverted Bouguer gravity data (Gao
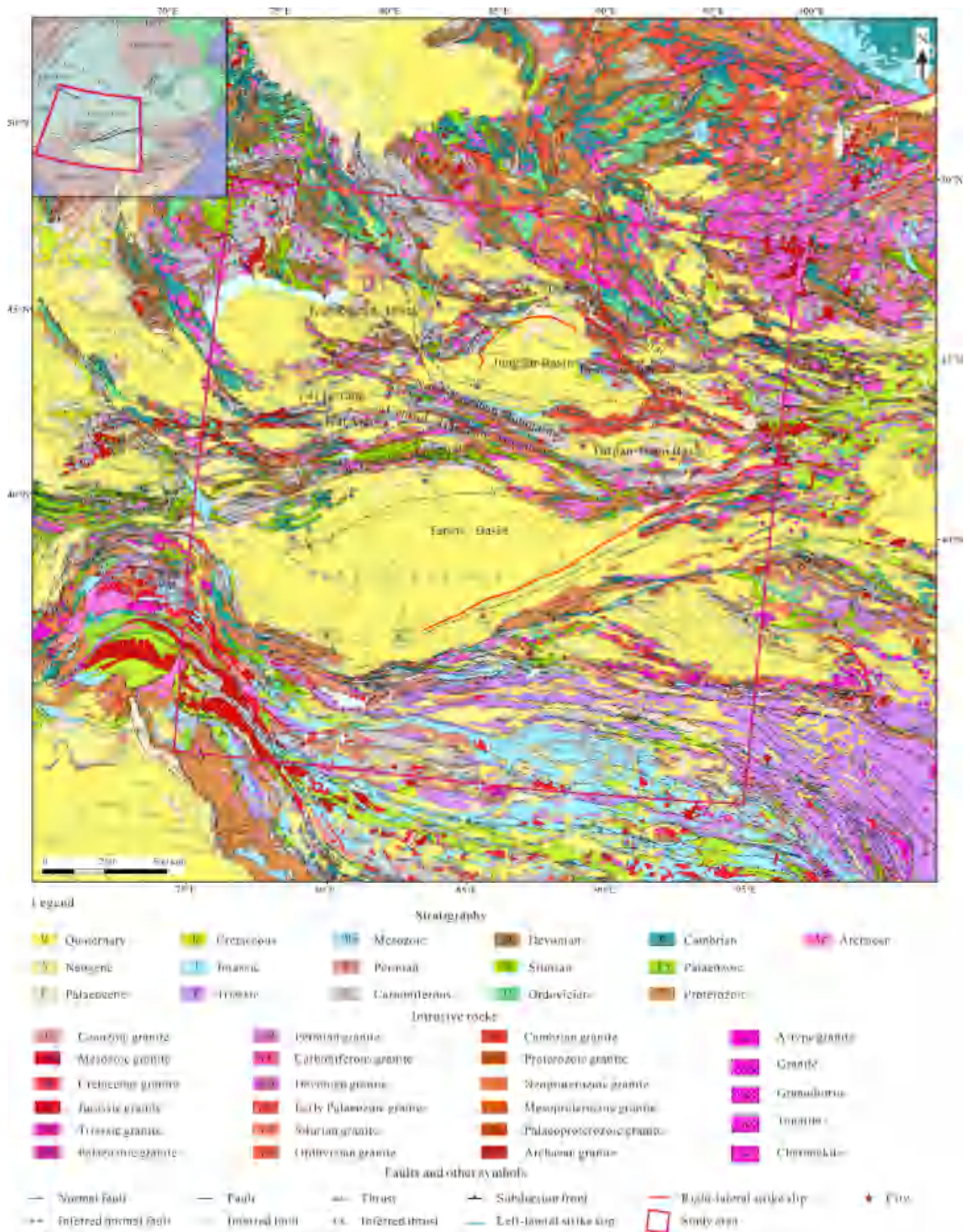

Fig. 1. Simplified geological map of the Chinese Altai, Junggar Basin, Tianshan Mountains, and Tarim Basin areas showing the extent of the study area (outlined in red) (modified after Ren, 2015; Chen et al., 2017; Wang et al., 2017). The latitude and longitude ranges of the area of the gravity data acquisition are 32.82–49.39°N and 73.61–97.97°E, respectively.

et al., 2001; He et al., 2001; An et al., 2018) and interpreted geological structures based on these data for the study area, which included the Altai Mountains, Junggar Basin, Tianshan Mountains, and Tarim Basin. We identified geophysical anomalies, determined the variation in the crustal material density, and constrained the presence and extent of the faults in this area. Our results provide insights into the geological structure and tectonic evolution of the investigated area and have implications for the formation of the southwestern CAOB.

2. Geological setting

The CAOB was constructed through the prolonged accretion of multiple microcontinents, island arcs, seamounts, oceanic plateaus, ophiolites, and accretionary complexes during the evolution of the Palaeo-Asian Ocean from the Neoproterozoic to the Late Palaeozoic, and it is considered one of the best examples of major Phanerozoic crustal growth (Jahn et al., 2000; Windley et al., 2007; Li et al., 2016). The southwestern CAOB consists of the Chinese Altai, Junggar, Tianshan, and Tarim units.

The Chinese Altai Orogen is an Early Palaeozoic juvenile magmatic arc terrane and is a very important accretionary orogen (Wang et al., 2021). The tectonic scenario for the accretionary orogens includes Neoproterozoic–Early Palaeozoic passive continental margin, the development of a Late Silurian to Early Devonian arc environment with a Middle Devonian back-arc basin, and continent–arc collision at the beginning of Late Devonian (Jiang et al., 2015; Wei et al., 2007; Kong et al., 2022). The Altai accretionary wedge records polyphase Palaeozoic deformation, metamorphic and magmatic events (Zhang et al., 2015; Jiang et al., 2021; Tian et al., 2021; Wang et al., 2021; Kong et al., 2022). The orogen comprises a variety of deformed and metamorphosed sedimentary formations, volcanic rocks, and granitic intrusions (Wang et al., 2006; Sun et al., 2008; Wang et al., 2009; Xiao et al., 2010; Li et al., 2021), and the granitic rocks occupy a large area of the Chinese Altai (~40%) (Jiang et al., 2014).

The Junggar region, which is surrounded by the Altai Orogen to the north, the Kazakhstan Plate to the west, and the Tianshan Mountains to the south (Zhou et al., 2018), is composed of Palaeozoic continental margin sequences and volcanic, ophiolitic, sedimentary, and intrusive rocks (Xiao et al., 2013; Li et al., 2015). The Junggar Basin formed during the Late Palaeozoic and evolved through foreland basin, intracontinental depression, and rejuvenated foreland basin stages (Xiao et al., 2008; Su et al., 2006). The Ordovician strata in the basin comprise a series of extremely thick pyroclastic rocks intercalated with siliceous and volcanic rocks (Gao et al., 2018). These are unconformably overlain by Carboniferous deposits composed of volcaniclastic turbidites covering pre-Carboniferous ophiolite mélange (Geng et al., 2009). The Permian rocks include continental volcanic and pyroclastic deposits, as well as molasse clastic deposits (Gao et al., 2018). The Triassic strata comprise a set of typical fluvial-lacustrine and swamp facies clastic deposits, which are conformably overlain by Jurassic coal-bearing strata. The Cretaceous mainly consists of clastic rocks, with minor interlayers of gypsum interposed locally (Xiao et al., 1994; Yang et al., 2012; Gao et al., 2019). The Cenozoic rocks comprise a sequence of continental clastic sedimentary rocks and Quaternary deposits, including those with alluvial, slope, aeolian, lacustrine, swamp, chemical, and glacial origins (Yang et al., 2012).

The Tianshan Mountains are composed of a series of E–W-trending subparallel mountain ranges and intermontane basins that have undergone multiple phases of tectonism and varying amounts of uplift (Molnar and Tapponnier, 1975; Tapponnier and Molnar, 1979; Allen et al., 1993, 1999; Charvet et al., 2011; Wilhem et al., 2012). The Archaean rocks in the Tianshan Mountains comprise marble, schist, granulite, and quartzite (Ma et al., 2014; Alexeiev et al., 2015, 2019). The Palaeoproterozoic rocks comprise greenschist to amphibolite facies plagioclase amphibolite, schist, quartzite, slate, phyllite, migmatite, granulite, and gneiss (Xiao et al., 2013; Ma et al., 2014; Gao et al., 2018). The

Cambrian rocks are dominated by neritic-shelf and platform facies carbonate rocks, clastic rocks, and siliceous rocks (Xiao et al., 2008) and are overlain by Ordovician strata, which primarily consist of clastic rocks, limestone, micrite, and mudstone (Mao et al., 2012). The Silurian strata are primarily composed of terrigenous clastic, pyroclastic, and carbonate rocks (Xiao et al., 1994; Gao et al., 2019; Hegner et al., 2020; Zhang et al., 2021). The Devonian strata predominantly consist of clastic, pyroclastic, carbonate, siliceous, and igneous rocks (Xiao et al., 1994; Gao et al., 2019; Zhang et al., 2021; Ye et al., 2022). The Carboniferous rocks include bimodal igneous, clastic, pyroclastic, and carbonate rocks (Qiu, 1989; Abuduxun et al., 2021). The Permian rocks are mainly composed of clastic, pyroclastic, and igneous rocks (de Jong et al., 2009; Abuduxun et al., 2021; Ye et al., 2022) and are overlain by Triassic rocks, which comprise lacustrine and fluvial clastic rocks (Xiao et al., 1994; Gao et al., 2019; Mao et al., 2022). The Jurassic strata consist of fluvial, lacustrine, and swamp facies clastic rocks, which are conformably overlain by Cretaceous piedmont-fluvial-lacustrine clastic rocks (Xiao et al., 1994; Gao et al., 2019). The Quaternary cover consists of alluvial, slope, aeolian, lake, swamp, chemical, and glacial deposits (Yang et al., 2012).

The Tarim Craton is composed of Archaean to Palaeoproterozoic basement, which is mainly composed of migmatitic granitoid gneisses and paragneisses, amphibolites, and mafic-intermediate intrusions (Zhang et al., 2012; Xu et al., 2013; Ge et al., 2018). The craton has a thick Mesoproterozoic to Phanerozoic cover, including siliciclastic and volcanic rocks (Lu et al., 2008; Zhu et al., 2011; Abuduxun et al., 2021). The Palaeozoic strata primarily consist of shallow-marine carbonate sedimentary and terrigenous clastic rocks and are overlain by Mesozoic sandstones and conglomerates (Carroll et al., 2013; Abuduxun et al., 2021). The Silurian to Permian strata mainly include mafic to felsic volcanic and intrusive rocks, sandstones, and conglomerates (Qu et al., 2003; Turner et al., 2010; Tian et al., 2010; Yang et al., 2013; Abuduxun et al., 2021).

3. Density of rock samples

Gravity anomalies are related to the spatial distribution of the density, and thus the density statistics of rocks and ores are important for identifying and interpreting Bouguer gravity anomalies (Zhu et al., 2022b). The density characteristics of a large number of rock samples acquired from the Chinese Altai, Junggar Basin, Tianshan Mountains, and adjacent areas during this study were measured at the China University of Geosciences (Wuhan) (Table 1).

The rock density is a function of various properties, including the mineral composition and contents, the structure and crystallinity of the minerals, the porosity, the composition and contents of the pore-filling materials, and the burial depth and environment. A higher rock density is typically associated with a higher proportion of dense minerals, a greater degree of crystallinity, a greater burial depth, and a lower temperature (Zhu et al., 2022b).

The rocks from the Chinese Altai, Junggar Basin, Tianshan Mountains, and adjacent areas exhibit a wide range of densities (Table 1). Ore and ferromagnetic minerals such as those in chrome ore, magnetite, pyrite, gabbro, porthyritic diabase, mafic volcanic rocks, diabase, basalt, and serpentine have very high densities. Most intrusive and extrusive igneous rocks have moderate but highly variable densities, including diorite porphyrite, tuff, diorite, basaltic porphyrite, andesitic porphyrite, granite porphyry, granodiorite, albitite, monzonite granite, granite, syenite porphyry, and K-feldspar granite.

In general, the density increases as the contents of the minerals increase from felsic to intermediate to mafic–ultramafic rocks. Plutonic rocks tend to be denser than metamorphic rocks, and metamorphic rocks tend to be denser than volcanic rocks. Sedimentary rocks typically have relatively low densities, including sandstone, siltstone, feldspathic quartz sandstone, feldspathic sandstone, siliceous rock, and mudstone. The density of sedimentary rocks is determined by the material composition, structure, burial depth, and porosity, with higher densities

Table 1

Densities of rock and ore samples from the Chinese Altai, Junggar Basin, Tianshan Mountains, and adjacent areas.

Sample number	Lithology	Number of samples	Density (g/cm^3) Range	Mean
1	Mudstone	31	2.525–3.089	2.770
2	Medium-grained sandstone	7	2.418–2.706	2.547
3	Siliceous rock	108	2.534–2.858	2.692
4	Feldspathic quartz sandstone	12	2.568–2.820	2.728
5	Feldspathic sandstone	57	2.724–2.804	2.761
6	Tuffaceous fine sandstone	3	2.708–2.764	2.729
7	Tuffaceous siltstone	189	2.550–2.881	2.689
8	Siltstone	1011	1.065–3.155	2.677
9	Sandstone	14	2.587–3.006	2.757
10	Lithic tuff	3	2.628–2.769	2.718
11	Rhyolite	23	2.572–2.691	2.626
12	Andesite	4	2.711–2.808	2.751
13	Rhyolitic andesite	3	2.601–2.617	2.609
14	Rhyolitic porphyry	6	2.551–2.786	2.712
15	Andesite porphyry	3	2.625–2.764	2.705
16	Andesitic porphyrite	15	2.591–2.697	2.653
17	Basaltic porphyrite	4	2.669–2.693	2.676
18	Porphyritic diabase	5	2.906–2.947	2.926
19	Mafic lava	13	2.635–3.228	2.883
20	Basalt	95	2.604–3.252	2.839
21	Granite porphyry	12	2.594–2.645	2.606
22	Tuff	17	2.622–2.740	2.704
23	Diorite porphyrite	20	2.621–3.024	2.768
24	K-feldspar granite	162	2.486–2.773	2.610
25	Syenite porphyry	3	2.611–2.612	2.612
26	Granite	752	2.380–3.035	2.620
27	Monzonite granite	71	2.525–2.753	2.641
28	Diorite	111	2.587–2.847	2.715
29	Granodiorite	4	2.637–2.664	2.657
30	Albitite	8	2.609–2.664	2.632
31	Gabbro	24	2.613–3.983	2.935
32	Diabase	82	2.650–3.140	2.878
33	Serpentine	68	2.527–3.260	2.725
34	Pyrite	8	2.691–3.298	3.042
35	Chrome ore	14	2.908–3.911	3.360
36	Magnetite	3	3.022–3.149	3.071

being associated with a greater burial depth and lower porosity.

4. Gravity data collection, processing, and inversion

The Bouguer gravity data used in this study (Gao et al., 2001; He et al., 2001; An et al., 2018), which are presented at the 1:100,000 scale, were acquired by the former Ministry of Geology and Mineral Resources of the People's Republic of China and are owned by the China Geological Survey (Fig. 2a). The latitude and longitude ranges of the data acquisition area are 32.82–49.39°N and 73.61–97.97°E, respectively. The mean square deviation of the gravity data is less than 3×10^{-5} m/s^2. The normal gravity field (γ_0) was calculated using the Helmert gravity formula:$\gamma_0 = 978030 \times (1 + 0.005302\sin^2\phi - 0.000007\sin^2 2\phi) \times 10^{-5}$m/s^2, where φ is latitude.

Various processing procedures were used to suppress the noise, extract and strengthen the useful information, and enhance the geological interpretation of the measured Bouguer anomalies. We conducted upward continuation, derivative calculation (Wang et al., 2010; Zhu et al., 2022b), and signal amplitude analysis (Zhu et al., 2018, 2019) using the ModelVision (V14.0) software during the gravity data processing (Zhu and Lu, 2016, 2021; Zhu et al., 2022b, 2022c). A detailed description of these processing procedures has been presented by Zhu et al. (2022b). The upward continuation procedure transforms the gravity data to make it appear as if they were collected at a greater height than was actually the case (Zhu et al., 2022b). This transformation can weaken high-frequency signals and constitutes low-pass

filtering of the gravity data. In this study, we conducted an upward continuation procedure for heights of 5, 10, 20, 40, and 60 km. We calculated the second derivative in the vertical dimension and conducted signal amplitude analysis using both the original gravity data and the data obtained by applying the upward continuation procedure for different heights (Zhu et al., 2018, 2019).

Here, we present a brief description of the 3-D gravity inversion methodology used in this study. When there are n observations and m rectangular prisms, the discrete forward modelling operator for gravity can be expressed in matrix form as follows:

$$g_{n \times 1} = G_{n \times m}\rho_{m \times 1} \tag{1}$$

where g is the vector of the observed data, ρ is the density distribution, and G is the gravity forward kernel function.

Geophysical inversion problems can be regarded as mathematical procedures for minimising data misfits in general. Because the solutions of geophysical inverse problems are non-unique and unstable (Tikhonov and Arsenin, 1977), we needed to regularise the problem with constraints, and the regularisation parameters were selected according to the adaptive method (Zhdanov, 2002). We also used a weighting function based on a sensitivity matrix, which uses only the kernel function matrix and can effectively solve the 'skin effect' of the inverted densities concentrated at the surface (Li and Oldenburg, 1996, 2000). For the regularised inverse problem, the expression of the model objective function was defined as (Ma et al., 2019):

$$minP^\alpha(\rho) = \varnothing(\rho) + \alpha S(\rho) = \|G\rho - g\|_2^2 + \alpha\|W_j(\rho)\|_2^2 \tag{2}$$

where $\varnothing(\rho)$ is the fitting function of the observed and predicted data, $S(\rho)$ is the stability function, and $W_j(\rho)$ is the weighting function. α is the regularisation parameter and can be expressed as follows (Ma et al., 2019):

$$\begin{cases} \alpha_1 = \varnothing(\rho)/S(\rho) \\ \alpha_k = \alpha_1/2^{k-1}, (k = 2, 3, \cdots, n) \end{cases} \tag{3}$$

The weighting function can be expressed as follows:

$$W_j = \left(\sum_{i=1}^{N} G_{ij}^2 \right)^{\beta/4} \tag{4}$$

where G_{ij} is an element of the gravity forward kernel function; i and j are the observation point number and model grid point number, respectively; and β is a constant whose value is usually set to 1 and can be used to control the strength of the weighting function.

5. Bouguer gravity anomaly characteristics and lithospheric structure

Bouguer gravity data are gravity data that have been treated for normal field correction, terrain correction, and Bouguer correction of the measured gravity data. Bouguer gravity anomalies reflect the spatial distribution of the geological bodies and the density and structural inhomogeneity of their constituent materials. The regional distribution of Bouguer anomalies represents the spatial variation in the structure and density of the crust and upper mantle.

The Bouguer anomalies in the Chinese Altai, Junggar Basin, Tianshan Mountains, and Tarim Basin regions are generally negative and exhibit complex spatial variations (Fig. 2). The central part of the study area is dominated by the low Bouguer anomalies in the western Tianshan Mountains and high Bouguer anomalies in the surrounding areas in the Bachu–Taklimakan Desert, Kuruktag Mountains, and Junggar Basin. In the outer parts of the study area, the Kunlun Mountains and Chinese Altai are characterised by relatively low Bouguer anomalies (Fig. 2). The lowest Bouguer anomalies are distributed in the area from the Karakorum Range to the Quanshuigou region in the southwestern part of the study area and are also present in the southeastern part of the study
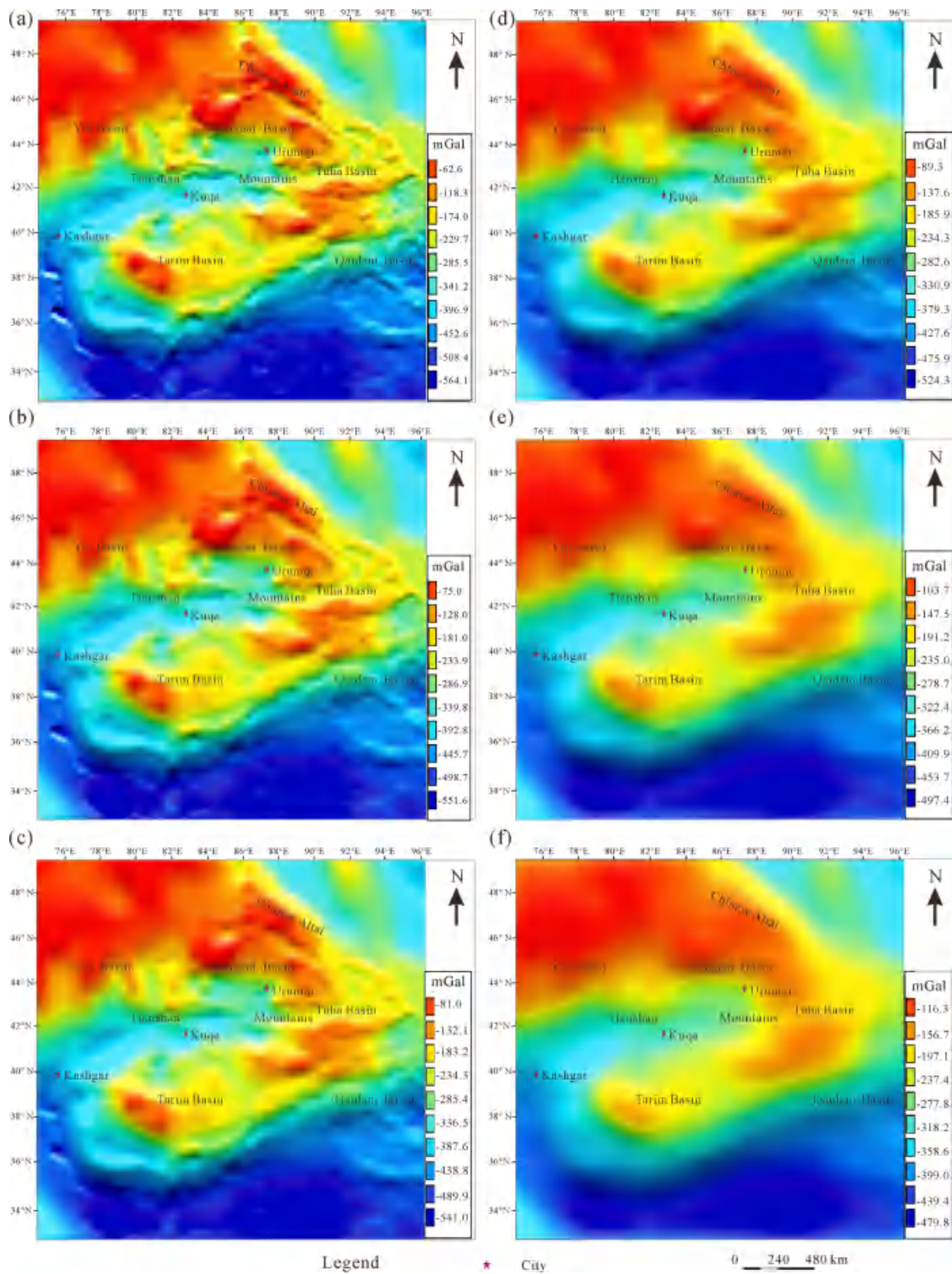
Fig. 2. (a) Distribution of the Bouguer gravity anomalies in the study area, including the Chinese Altai, Junggar Basin, Tianshan Mountains, and Tarim Basin areas; Processed upward continuation maps for heights of (b) 5 km, (c) 10 km, (d) 20 km, (e) 40 km, and (f) 60 km (unit: mGal). The red stars mark the locations of cities.

area. From the southeast to the north, they gradually increase toward the Tarim Basin (Fig. 2). The highest local Bouguer anomalies are distributed in the northwestern margin of the Junggar Basin.

An area with low Bouguer anomalies extends from the north of the Chinese Altai–Fuyun fault to the south of the Ermantai fault zone, and the Bouguer anomalies in the central part of the Fuhai–Salkaren region are high (Fig. 2). The Bouguer anomalies in the Chinese Altai exhibit a NW–SE-trending pattern (Figs. 3 and 4). The distribution of the anomaly gradient belt in this region is consistent with the main tectonic structures there. The Bouguer anomalies in the Fuhai area are relatively high and gradually decrease eastward. The anomalies on the western side of the Chinese Altai show E–W- and NNE–SSW-trending patterns, whereas those on the eastern side exhibit NW–SE-trending patterns (Figs. 3 and 4). The Bouguer anomalies in the Xibodu area vary only slightly and exhibit a NW–SE-trending pattern. The low Bouguer anomalies in the southern part of the Fuhai and Fuyun regions gradually disappear with increasing upward continuation height (Fig. 2b–f), and the Chinese Altai are characterised by generally high Bouguer anomalies at an upward continuation height of 60 km.

The Bouguer anomalies in the Junggar Basin exhibit NW–SE-trending pattern, and the anomalies decrease from north to south (Figs. 3 and 4). The Bouguer anomalies are typically high in the central mountains and low in the basin, forming a marked Bouguer anomaly gradient zone in the piedmont and demonstrating a negative correlation with the spatial distribution of the topography (Fig. 2). The Bouguer anomalies in western Junggar are very high and exhibit a disrupted pattern. The Zaloule Mountains are dominated by relatively low Bouguer anomalies, and the anomaly gradient belt in this region reveals that there is a smooth transition zone between the uplifted and downthrown rock masses (Fig. 2). The Bouguer anomalies in Karamay are high and exhibit a NE–SW-trending pattern (Figs. 3 and 4). With increasing upward continuation height, the low Bouguer anomalies in the Junggar Basin gradually intensify, and the difference between the anomalies in the western part of the basin and those in the Karamay area gradually decreases (Fig. 2b–f). The high anomalies in the northern part of the basin and those in the Chinese Altai region merge at an upward continuation height of 60 km.

The Tianshan Mountains can be divided into an area of low Bouguer anomalies in the western part of the mountains and an area of high anomalies in the eastern part, and these areas are separated by an approximate boundary along the line between Urumqi and Korla (Fig. 2). There are several regional Bouguer anomaly gradient belts in this area (Figs. 3 and 4). Taking the line between Urumqi and Korla as the eastern boundary of the western Tianshan Mountains, the Bouguer anomalies in this region generally exhibit a NW–SE-trending pattern and gradually increase from the central Tianshan Mountains toward both sides of the range (Figs. 3 and 4). The Bouguer anomalies in the Bole area are relatively high and are inferred to represent basement uplift and the presence of magmatic rocks in this area. The Bouguer anomalies in the Yining area are low and exhibit a NW–SE-trending pattern, which differs from the high anomalies and E–W-trending pattern in the Gongliu–Xinyuan area (Figs. 3 and 4). The Bouguer anomalies in the Tashiyuyi–Hejing area are generally low and distributed in a NE–SW-trending pattern, whereas those in the Kalpin–Aksu area are mainly high and also exhibit a NE–SW-trending pattern (Figs. 3 and 4). The negative anomalies in the Yining area gradually decrease with increasing upward continuation height (Fig. 2b–f), and the negative anomalies to the south of Kuytun and Urumqi merge with the anomalies on the northern side of Kuqa at an upward continuation height of 60 km.

The Bouguer anomalies in the eastern Tianshan Mountains display an E–W-trending pattern and are dominated by regional high anomalies with superimposed local low anomalies (Figs. 3 and 4). The Bouguer anomalies are high and exhibit an E–W-trending pattern in the Harlik Mountain area, and they gradually decrease from west to east. The Bouguer anomalies are low and exhibit a nearly E–W-trending pattern in the Turpan–Hami Basin area, and they gradually increase with

increasing upward continuation height (Fig. 2b–f). The two areas with high Bouguer anomalies in the northern and southern parts of the eastern Tianshan Mountains merge at an upward continuation height of 60 km.

The Bouguer gravity anomalies vary slightly in the Tarim Basin compared with the more marked variation at the edge of the basin (Fig. 2). The trends of a series of large-scale Bouguer gravity anomalies around the basin correspond to the strikes of the basin boundaries and differ substantially from the strikes of the faults in the basin. Pronounced Bouguer anomaly gradients are present in the southeastern margin of the Tarim Basin (Fig. 2b–f). A NE–SW-trending anomaly gradient belt is observed in the Kuqa–Aheqi–Atushi area in the western part of the northern margin of the basin, and a NW–SE-trending gradient belt is present in the western part of the southern margin (Figs. 3 and 4). The Bouguer anomalies are mainly high in the central part of the Tarim Basin and show a NNE–SSW-trending pattern, whereas those in the northern and southwestern parts of the basin are relatively low. The values and spatial patterns of the Bouguer anomalies on the two sides of the basin bounded by longitude 82°E are very different (Fig. 2). The Bouguer anomalies in the basin to the west of this meridian exhibit complex variations, and a NNW–SSE-trending Bouguer gravity gradient occurs along latitude ∼ 40°N. The gradient is greater on the northern side than on the southern side (Figs. 3 and 4). By contrast, the anomalies to the east of the meridian vary only slightly.

NNE–SSW-, NW–SE-, and nearly E–W-trending faults mainly occur in the basement around the Tarim Basin (Figs. 3 and 4). The northern margin of the basin is dominated by NNE–SSW-trending faults, and the southwestern margin is dominated by NW–SE-trending faults. There is a NE–SW-trending regional strike-slip fault zone in the southeastern margin of the basin and there are two sets of faults (NE–SW- and E–W-trending) in the northeastern part of the basin (Figs. 3 and 4).

We carried out 3-D inversion of the gravity data for the region across the Chinese Altai Orogen, Junggar Basin, Tianshan Orogen, and Tarim Basin using the GeoProbe (V4.0) software developed by the China Geological Survey. The defined study area measured ∼ 1810 × 1770 km, and the target depth range of the Bouguer gravity anomalies extended from the surface to an elevation of − 80 km. We chose the size of the 3-D grid according to the requirements of the scale of the data, the inversion accuracy, and the calculation efficiency. We adopted a spline interpolation gridding method during the modelling process, with a total of 647,920 grid points in the mesh data. We established an initial density model based on the measured density variations of the rocks and ores (Table 1).

The 3-D density inversion results reveal the spatial distribution of the material density in the Chinese Altai, Junggar Basin, Tianshan Mountains, and Tarim Basin (Figs. 5 and 6). The distribution of the lithospheric structures shown in Figs. 5 and 6 was collated from the faults and structures interpreted from the gravity patterns described above and those identified and interpreted in Figs. 3 and 4. A total of 23 deep regional faults (F1–F23 in Table 2) and numerous other faults were identified and are mapped in Fig. 7. The high-density regions are consistent with the regions with high Bouguer anomalies (Fig. 2). According to the slices at different depths (Fig. 5), the high-density regions in the Tianshan Mountains, Chinese Altai, and Junggar areas gradually shrink with increasing model depth. The distribution range of the high-density areas in the Tarim Basin gradually shrinks with increasing model depth, whereas the distribution range of the low-density areas to the south of the basin gradually expands. The variation in the density with depth is consistent with the variation in the Bouguer gravity anomalies with increasing upward continuation height (Fig. 2b–f).

6. Discussion

6.1. Crustal characteristics of the Chinese Altai–Junggar Basin area

The crustal thickness of the southern margin of the Chinese Altai
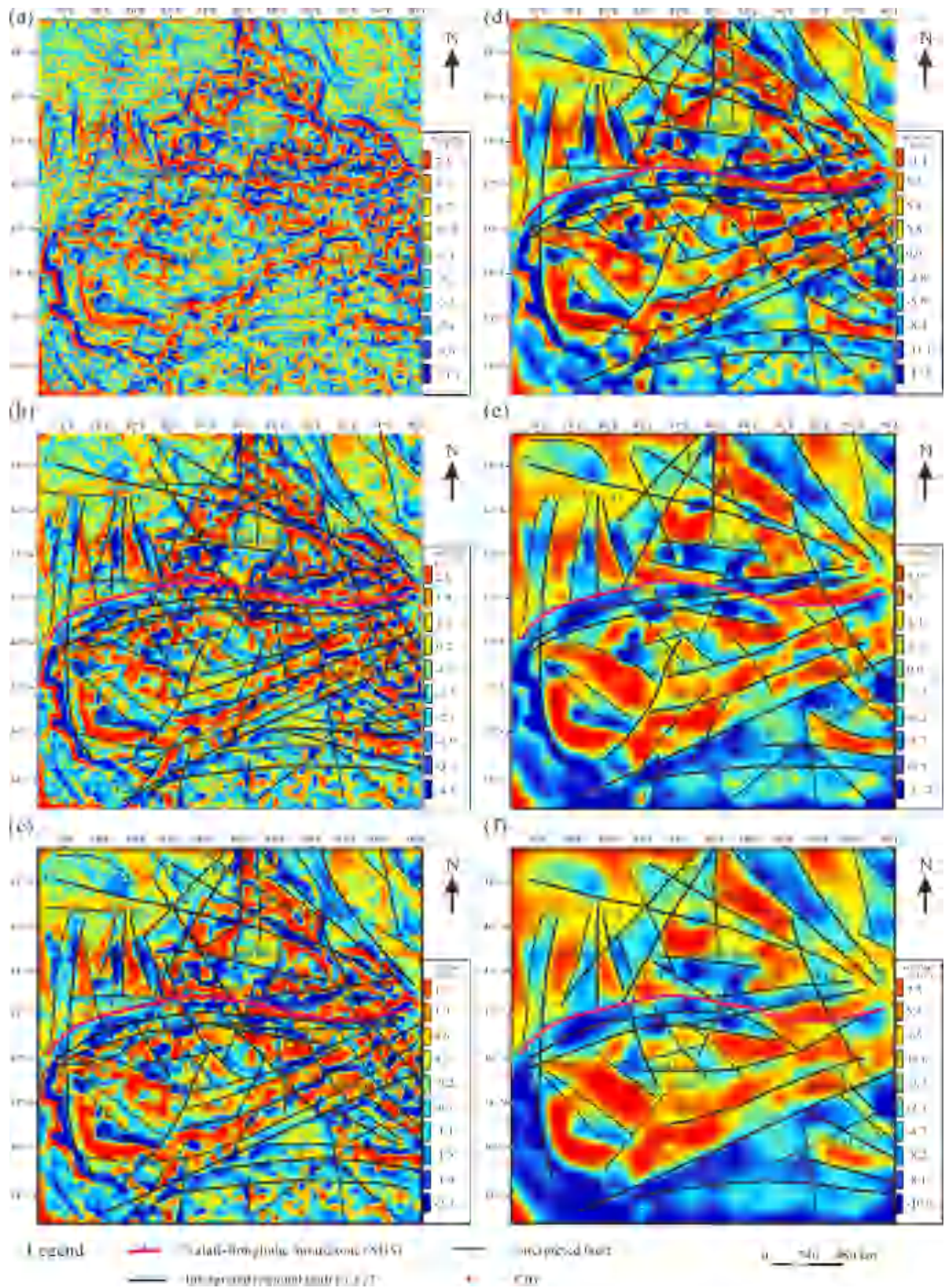
Fig. 3. (a) Second-order derivative in the vertical direction of the Bouguer gravity anomaly map; Processed upward continuation maps for heights of (b) 5 km, (c) 10 km, (d) 20 km, (e) 40 km, and (f) 60 km (unit: mGal/m²). The regional faults (thick black lines, see Table 2), fault systems (thin black lines), and the Nalati–Hongliuhe Suture zone (red line) are also shown.
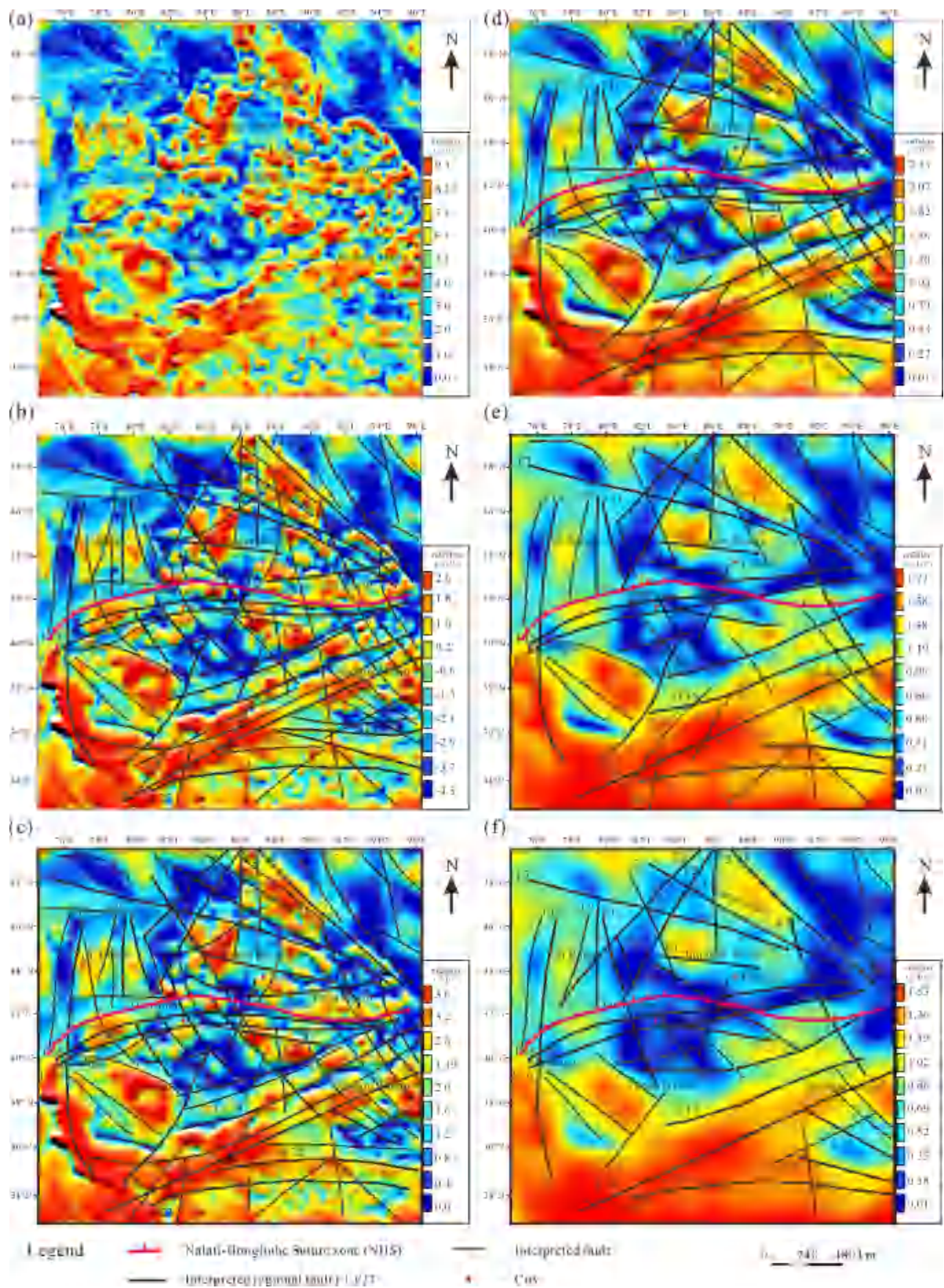
Fig. 4. Signal amplitude of the Bouguer gravity anomaly map (a); Processed upward continuation maps for heights of (b) 5 km, (c) 10 km, (d) 20 km, (e) 40 km, and (f) 60 km (unit: mGal/m). The regional faults (thick black lines, see Table 2), fault systems (thin black lines), and the Nalati–Hongliuhe Suture zone (red line) are also shown.
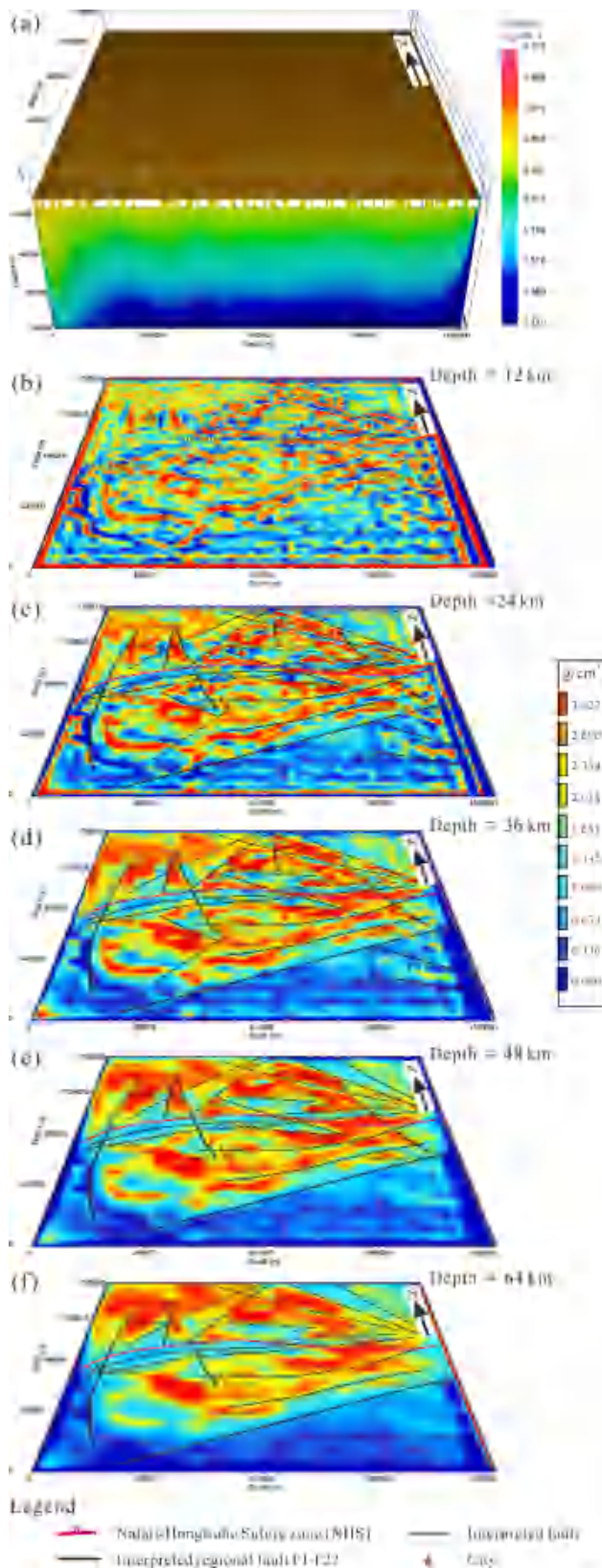
Fig. 5. (a) Spatial distribution of density obtained from 3-D gravity inversion; Density sections at depths of (b) 12 km, (c) 24 km, (d) 36 km, (e) 48 km, and (f) 64 km. The interpreted faults are those shown in Fig. 3.
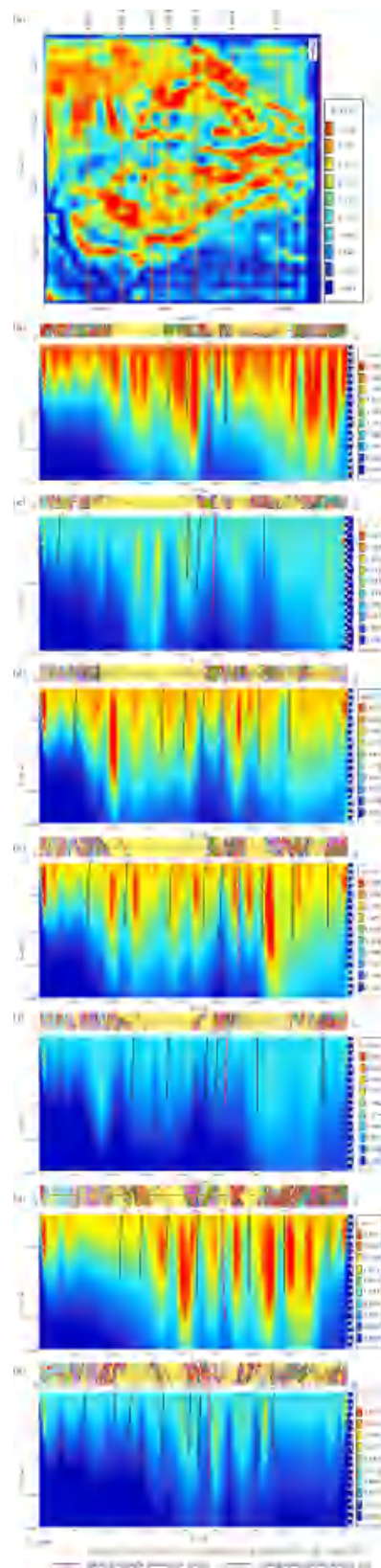
Fig. 6. Sections of 3-D inversion results. (a) Schematic diagram showing the locations of the seven N–S sections across the study area; (b–h) distribution of material density along sections 1–7, respectively. The surface geology for each section is from Fig. 1.

Table 2

Regional faults and their characteristics based on Bouguer gravity data for the Chinese Altai orogen, Junggar Basin, Tianshan Mountains, and Tarim Basin.

Fault name	Fault strike	Characteristics of the gravity field
NHS	ENE–WSW	Collision and extrusion belt, accretionary plateau contact belt
F1	NE–SW	Gradient variation belt, discontinuity and dislocation belt
F2	NE–SW	Gradient variation belt, accretionary complex belt
F3	S–N	Bead-like anomaly belt, discontinuity and dislocation belt
F4	SE–NW	Gradient variation belt, collision and extrusion belt
F5	SE–NW	Gradient variation belt, accretionary complex belt
F6	SE–NW	Gradient variation belt, accretionary complex belt
F7	SE–NW	Gradient variation belt, accretionary complex belt
F8	SSE–NNW	Bead-like anomaly belt, accretionary complex belt
F9	S–N	Gradient variation belt, accretionary complex belt
F10	S–N	Gradient variation belt, fault basin junction belt
F11	SSE–NNW	Gradient variation belt, fault basin junction belt
F12	E–W	Gradient variation belt, fault basin junction belt
F13	SE–NW	Gradient variation belt, fault basin junction belt
F14	E–W	Bead-like anomaly belt, subduction complex belt
F15	E–SSW	Bead-like anomaly belt, collision and extrusion belt
F16	NNE–SSW	Bead-like anomaly belt, collision and extrusion belt
F17	E–NNW	Gradient variation belt, collision and extrusion belt
F18	NE–W	Bead-like anomaly belt, discontinuity and dislocation belt
F19	NNE–SSW	Gradient variation belt, collision and extrusion belt
F20	NE–SW	Gradient variation belt, accretionary plateau contact belt
F21	SE–NW	Bead-like anomaly belt, discontinuity and dislocation belt
F22	SSE–NNW	Gradient variation belt, accretionary complex belt
F23	W–E	Gradient variation belt, accretionary complex belt

varies between ~ 30 and ~ 55 km (Laske et al., 2021; Zhu et al., 2022a). There is a partially molten mantle low-resistivity layer at a depth of ~ 70 km and it is much shallower than the normal depth (Liang et al., 1999). This indicates the occurrence of tectonic activity in the lithosphere and the possible existence of multiple tectonic detachment layers in this area (Figs. 5 and 6) (Liang et al., 1999). The thick lower crust in the Chinese Altai implies that crustal thickening was accompanied by the deepening of the Moho to the north and uplift of the upper crust (Wang et al., 2004; Laske et al., 2021; Zhu et al., 2022a). The distribution of the ore deposits in the Chinese Altai (Wang et al., 2023a, 2023b) reveals that most of these deposits are located on the boundaries between the high Bouguer anomalies in the central part of the Chinese Altai and the low anomalies in the southern part, that is, in the steep Bouguer gravity anomaly gradient belt (close to F6) (Figs. 2–4) (Zhu et al., 2021). This observation is consistent with the results of whole-rock Nd and zircon Hf isotope mapping, which have revealed the spatial distributions of three types of deposits (Wang et al., 2023a, 2023b).

The crustal structure in the Junggar Basin can be divided into several parts (Figs. 5 and 6). The General's Temple area, which is located in the central part of the basin, is characterised by high-density materials at depth, possibly representing Palaeozoic oceanic crust transformed directly into the continental crust during the process of mantle intrusion into the lower crust (Figs. 5 and 6). This result is consistent with the resistivity cross sections obtained from magnetotelluric data (Xu et al., 2016, 2020). The basement of the Junggar Basin is shallow in the north and deep in the south. There may be a series of nappe structures in the area to the north of the General's Temple, and the strata in the northern part of the basin exhibit nappe–thrust structures with south-to-north movement. The middle-lower crust and upper mantle in the northern Junggar Basin are characterised by high-density materials with a tendency to plunge to the north, which is consistent with the northward subduction of a palaeo-oceanic slab beneath the lithosphere of the Chinese Altai (Figs. 5 and 6) (Xu et al., 2015). The Karamaili tectonic

zone in the southern part of the basin is considered a Middle Carboniferous suture zone between the Siberian and Kazakhstan plates (Li et al., 1988; Wu et al., 2006). The high-density region that extends southward to the northern Tianshan Mountains may represent the lithosphere of the ancient Junggar oceanic basin and the northward subduction of the Kazakhstan Plate under the Siberian Plate (Figs. 5 and 6) (Liang et al., 1999; Xu et al., 2015).

The consistent high-density characteristics of the Junggar Basin imply a relatively complete crust–mantle structure (Figs. 5 and 6) (Wang et al., 2004). The ancient Junggar oceanic crust may have subducted toward the NE and NW under the Siberian Plate and the West Junggar block, respectively (Xu et al., 2015). The high-density materials may represent the lithosphere of the ancient Junggar Ocean, which extends southward below the northern Tianshan Mountains (Figs. 5 and 6). The existence of high-density materials on the southern side of the Erqis fault may indicate the intrusion of mantle material (e.g., ultramafic materials) along this deep lithospheric-scale fault or overlapping and thickening of oceanic crust via an intra-oceanic nappe shear (Figs. 5 and 6) (Liang et al., 1999).

The high Bouguer gravity anomalies in West Junggar and the surrounding areas indicate that the Junggar orogenic belt is not composed of strongly folded and deformed strata but of ophiolite mélange (Figs. 2–4) (Tian and Yang, 2015; Yang et al., 2015). Broadband seismic observations provide support for NW–SE oriented palaeo-subduction in which an oceanic slab became trapped beneath southwestern Junggar (Wu et al., 2018). Early Palaeozoic Junggar oceanic crustal material may still be retained in the middle and lower crust in the northwestern margin of the basin. During the Late Carboniferous, the subduction direction of the Junggar oceanic plate toward the Kazakhstan Plate was from SSE to NNW. The high density in the Karamay area may be related to the occurrence of mafic mantle-derived materials in the lower-middle crust, whereas the low density in the Tacheng area may represent the presence of thick Mesozoic–Cenozoic sediments (Figs. 5 and 6).

6.2. Nature of the basement of the Junggar Basin

The Junggar Basin is characterised by low Bouguer anomalies (Figs. 2–4), and the pattern of the anomalies only changes slightly with increasing depth. The basin also contains high magnetic anomalies (Zhu et al., 2022a). The Junggar Basin has deep Curie point depths (~30–42 km) in its centre and shallow depths in its western and eastern parts and northern margin, and it has a crustal thickness of ~ 40 km (Laske et al., 2021; Zhu et al., 2022a). The high density in the Karamay area may be related to the presence of mafic mantle-derived materials in the lower-middle crust. The isotope mapping results of Wang et al. (2023b) revealed that the igneous rocks from numerous drill holes in the Junggar Basin have primitive isotopic characteristics [$\varepsilon Nd(t) = +2$ to $+6$; median zircon $\varepsilon Hf(t) = +4$ to $+9$], which are similar to those of the igneous rocks around the basin. Nd and Hf isotope mapping and zircon xenocryst mapping of the igneous rocks in the eastern and western parts of the Junggar orogen have shown no evidence of the existence of a widespread ancient continental crustal basement (Zhang et al., 2017; Song et al., 2019; Wang et al., 2023a, 2023b). All of the abovementioned observations suggest that the basement of the Junggar Basin is composed of oceanic crustal materials.

6.3. Crustal features of the Tianshan Mountains

Both the deep crust and upper mantle in the Tianshan Mountains have low-density anomalies that extend into the basins to the north and south of the orogen (Figs. 5 and 6). Large-scale low-density bodies are inferred in the uppermost mantle at the contact between the Tarim Basin and Tianshan orogenic belt and the contact between the Junggar Basin and Tianshan orogenic belt (Figs. 5 and 6). The Moho depth in most parts of the Tianshan Mountains is less than 60 km, and the maximum value is ~ 62 km according to a deep seismic profile across the Tianshan
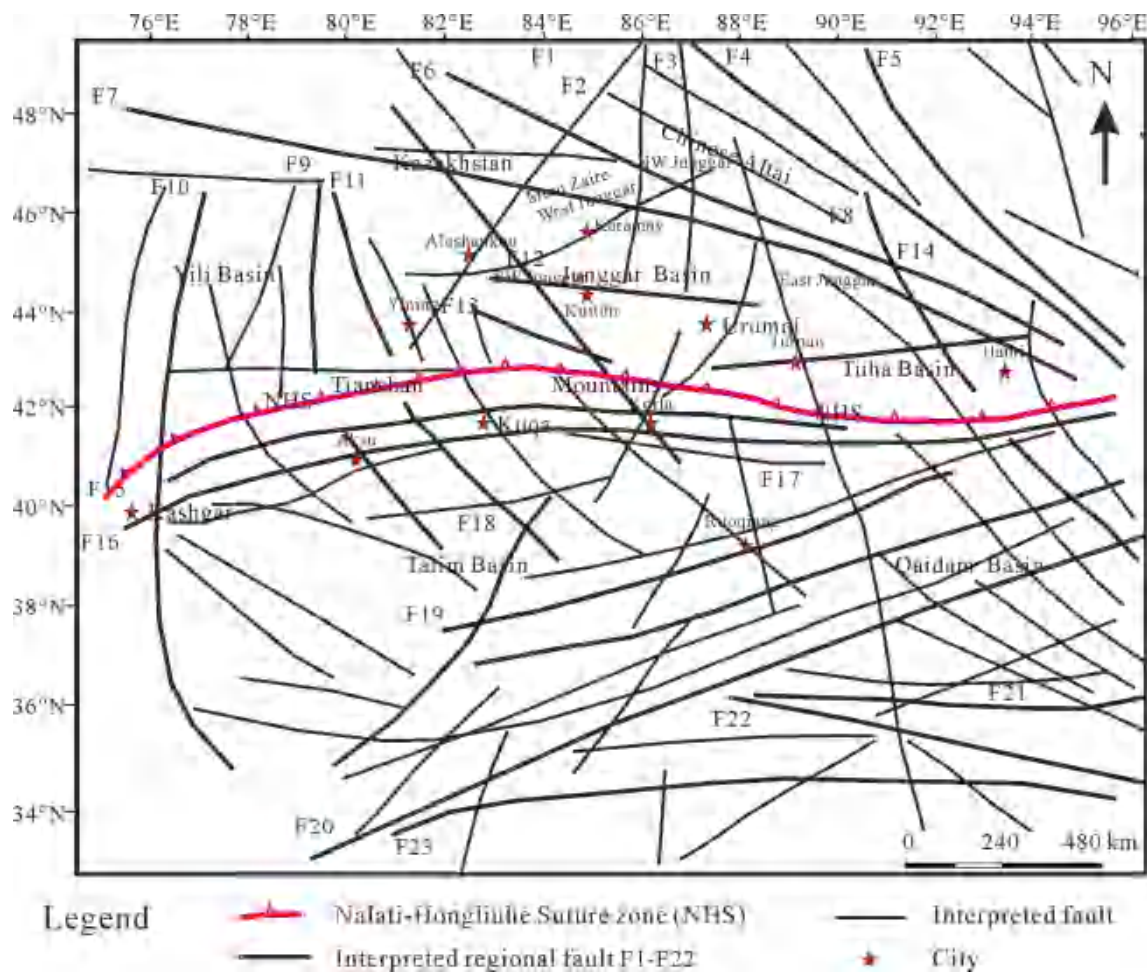
Fig. 7. Map showing the faults interpreted from the gravity measurements in the Chinese Altai, Junggar Basin, Tianshan Mountains, and Tarim Basin regions. NHS is the interpreted Nalati–Hongliuhe Suture zone, and the regional faults are labelled F1–F23.

Mountains (Lu et al., 2000). There are no obvious mountain roots beneath the Tianshan Mountains, and most of the crust and mantle therein correspond to transitional density gradient zones (Figs. 5 and 6) (Li et al., 2007). The crust in the Tianshan Mountains is composed of blocks (Fig. 6). The discontinuous structure of the crust and mantle interface indicates that there have been pronounced differential vertical movements between the different parts of the Tianshan Mountains. These differential movements may have been caused by the transport of lower crustal materials into the uppermost mantle of the Tianshan orogenic belt via interlayer insertion/subduction of the Tarim Block into/below the Tianshan orogenic belt, as well as subduction of the Junggar Block below the Tianshan orogenic belt (Figs. 5 and 6) (Liang et al., 1999; Zhao et al., 2004).

6.4. Nature of the basement of the Tarim Basin

The crustal thickness in the northern, western, and southern parts of the Tarim Basin increases markedly from the centre of the basin to the periphery, forming an annular spatial pattern of thick crust surrounding the basin (Yin et al., 1998; Xu et al., 2005; Laske et al., 2021; Zhu et al., 2022a). The crustal thickness in the Tarim Basin is uniform, but the individual thicknesses of the middle and upper crusts vary greatly. The crustal thickness exhibit an annular spatial pattern, withthinner (~40 km) crust in the basin and an abrupt increase to ~ 55 km in the area surrounding the basin (Figs. 5 and 6) (Laske et al., 2021; Zhu et al., 2022a), suggesting that the basement and Moho in the central and eastern parts of the Tarim Basin were uplifted relative to the other parts.

The mantle underlying the basin was uplifted in the Early Palaeozoic, causing the crust in the basin to become thinner, implying that the lithosphere in the Tarim Basin flexed and underwent deformation under compression as part of the far-field effects of the Indian–Asian plate collision (Zhu et al., 2011; Zhang et al., 2012). The structure of the upper mantle below the basin is consistent with the basement structure of the basin (Xu et al., 2005).

The results of zircon geochronological analysis of rocks from outcrops around the Tarim Basin have revealed that the basement of the basin is composed of Archaean–Palaeoproterozoic crystalline basement and Meso-Neoproterozoic metamorphic basement (Yang et al., 2014). These basement rocks exhibit pronounced regional differences in genesis and composition (Long et al., 2010b, 2011; Yang et al., 2014). The basement in the northern, central, and southern parts of the basin is composed of Meso-Neoproterozoic medium- and low-grade metamorphic rocks, Palaeoproterozoic granites, and Palaeoproterozoic paragneiss metamorphic rocks, respectively (Hu et al., 2001; Wu et al., 2012; Yang et al., 2014). The basement in the eastern and southeastern parts of the basin is composed of Archaean basaltic granulites and migmatites, including Palaeoproterozoic granite bodies, the Qingbaikou granites, and Neoproterozoic basalts (Wu et al., 2012; Yang et al., 2014).

The lithosphere in the Tarim Basin constitutes a rigid block with high seismic-wave velocities, high strength, and pervasive deformation. In contrast to the crust in the Tarim Basin, the crust in the Junggar Basin may not comprise a crystalline basement composed of a high-grade metamorphic rock series (Chen and Chen, 2002).

7. Conclusions

In this study, we investigated the Altai Orogen, Junggar Basin, Tianshan Orogen, and Tarim Basin using Bouguer gravity data to reveal the presence and distribution of the crustal structures. The Bouguer anomalies in the Chinese Altai and Junggar Basin exhibit a NW–SE-trending spatial pattern, and those in the Junggar Basin form three E–W-oriented high-anomaly belts. The Bouguer anomalies in the western Tianshan Mountains present a NW–SE-trending pattern, whereas those in the eastern Tianshan Mountains are oriented E–W. In the central Tarim Basin, the Bouguer anomalies vary only slightly, and a NNW–SSE-oriented Bouguer anomaly gradient belt occurs along $\sim 40°$N.

Gravity and density results suggest the existence of multiple tectonic detachment layers in the crust and upper mantle of the Chinese Altai Orogen. The basement of the Junggar Basin may be composed of oceanic crustal materials, and ancient Junggar oceanic crust may have been subducted to the NE and NW under the Siberian Plate and the West Junggar Block, respectively. There is no evidence of mountain roots in the crust in the Tianshan Mountains. The inferred low density of the lower crust and upper mantle in the Tianshan Mountains implies that lower-crustal materials may have been incorporated into the uppermost mantle beneath this orogen. The basement of the Tarim Basin is composed of Archaean–Palaeoproterozoic crystalline basement and Meso-Neoproterozoic metamorphic basement. Overall, our findings based on Bouguer gravity and material density data provide important insights into the deep crustal structures and tectonic evolution of the southwestern CAOB.

CRediT authorship contribution statement

Xiaosan Zhu: Conceptualization, Methodology, Data curation, Software, Investigation, Writing – original draft, Writing – review & editing. **Yusen Huang:** Software, Writing – original draft. **Tao Wang:** Resources, Writing – review & editing. **He Huang:** Resources, Writing – review & editing. **Hongwei Zheng:** Data curation, Visualization.

Declaration of Competing Interest

The authors declare that they have no known competing financial interests or personal relationships that could have appeared to influence the work reported in this paper.

Data availability

The authors do not have permission to share data.

Acknowledgements

References

Abuduxun, N., Xiao, W., Windley, B.F., Chen, Y., Huang, P., Sang, M., Li, L., Liu, X., 2021. Terminal suturing between the Tarim Craton and the Yili-Central Tianshan arc: Insights from melange–Ocean Plate Stratigraphy, detrital zircon ages, and provenance of the South Tianshan accretionary complex. e2021TC006705 Tectonics 40. https://doi.org/10.1029/2021TC006705.

Alexeiev, D.V., Biske, Y.S., Djenchuraeva, A.V., Kroner, A., Getman, O.F., 2019. Late Carboniferous (Kasimovian) closure of the South Tianshan Ocean: No Triassic subduction. J. Asian Earth Sci. 173, 54–60. https://doi.org/10.1016/j.jseaes.2019.01.021.

Alexeiev, D.V., Biske, Y.S., Wang, B., Djenchuraeva, A. V., Getman, O.F., Aristov, V.A., A. Liu, H., Zhong, L., 2015. Tectono-Stratigraphic framework and Palaeozoic evolution of the Chinese South Tianshan. Geotectonics 49(2), 93–122. https://doi.org/10.1134/S0016852115020028.

Allen, M.B., Windley, B.F., Zhang, C., 1993. Palaeozoic collisional tectonics and magmatism of the Chinese Tien Shan, central Asia. Tectonophysics 220 (1), 89–115. https://doi.org/10.1016/0040-1951(93)90225-9.

Allen, M.B., Vincent, S.J., Wheeler, P.J., 1999. Late Cenozoic tectonics of the Kepingtage thrust zone: Interactions of the Tien Shan and Tarim Basin, northwest China. Tectonics 18 (4), 639–654. https://doi.org/10.1029/1999TC900019.

An, S., Zhou, K., Wang, J., Yang, H., Zhang, Z., 2018. Integrated analysis of gravity and magnetic fields in the Eastern Tianshan Belt, Xinjiang, Central Asia: Implications for Cu-Au-Fe polymetallic deposits exploration. J. Appl. Geophys. 159, 319–328.

Carroll, A.R., Dumitru, T.A., Graham, S.A., Hendrix, M.S., 2013. An 800 million-year detrital zircon record of continental amalgamation: Tarim basin, NW China. Int. Geol. Rev. 55 (7), 818–829. https://doi.org/10.1080/00206814.2013.787232.

Charvet, J., Shu, L., Laurent-Charvet, S., Wang, B., Faure, M., Cluzel, D., Jong, K., 2011. Palaeozoic tectonic evolution of the Tianshan belt, NW China. Sci. China Earth Sci. 54 (2), 166–184. https://doi.org/10.1007/s11430-010-4138-1.

Chen, J., Chen, J., 2002. Basement of Junggar Basin and Its seismic velocity characteristics. XinJiang Petrol. Geol. 23 (6), 474–478 in Chinese with English abstract.

Chen, Y., Xiao, W., Windley, B.F., Zhang, J., Zhou, K., Sang, M., 2017. Structures and detrital zircon ages of the Devonian-Permian Tarbagatay accretionary complex in west Junggar, China: imbricated ocean plate stratigraphy and implications for amalgamation of the CAOB. Int. Geol. Rev. 59 (9), 1097–1115. https://doi.org/10.1080/00206814.2016.1185652.

Coleman, R.G., 1989. Continental growth of Northwest China. Tectonics 8 (3), 621–635.

de Jong, K., Wang, B., Faure, M., Shu, L., Cluzel, D., Charvet, J., Ruffet, G., Chen, Y., 2009. New 40Ar/39Ar age constraints on the Late Palaeozoic tectonic evolution of the western Tianshan (Xinjiang, northwestern China), with emphasis on Permian fluid ingress. Int. J. Earth Sci-Geol. Rundsch 98, 1239–1258.

Feng, Y., Coleman, R.G., Tilton, G., Xiao, X., 1989. Tectonic evolution of the west Junggar region, Xinjiang, China. Tectonics 8 (4), 729–752.

Gao, R., Guan, Y., He, R., Shi, D., Li, D., Li, Q., Lu, D., Li, L., 2001. The integrated geophysical observation and research along the Xinjiang (XUAR) geotransect and its surrounding areas. Acta Geosci. Sin. 22 (6), 527–533 in Chinese with English abstract.

Gao, G., Hou, J., Kang, G., Bai, C., Wen, L., Zhao, H., Shi, L., 2019. Crustal thickness and lithospheric thermal state beneath the Junggar Basin and adjacent Mountain Ranges, northwest China. J. Asian Earth Sci. 184, 103802.

Gao, J., Klemd, R., Zhu, M., Wang, X., Li, J., Wan, B., Xiao, W., Zeng, Q., Shen, P., Sun, J., Qin, K., Campos, E., 2018. Large-scale porphyry-type mineralization in the Central Asian metallogenic domain: A review. J. Asian Earth Sci. 165, 7–36.

Gao, R., Xiao, X., Kao, H., Li, Q., Liu, X., Jiang, M., Shi, D., 2002. Summary of deep seismic probing of the lithospheric structure across the West Kunlun–Tarim–Tianshan. Geol. Bull. China 21 (1), 11–20 in Chinese with English abstract.

Ge, R., Zhu, W., Wilde, S.A., Wu, H., 2018. Remnants of Eoarchean continental crust derived from a subducted proto-arc. Sci. Adv. 4 (2), eaao3159. https://doi.org/10.1126/sciadv.aao3159.

Geng, H., Sun, M., Yuan, C., Xiao, W., Xian, W., Zhao, G., Zhang, L., Wong, K., 2009. Geochemical, Sr-Nd and zircon U-Pb-Hf isotopic studies of Late Carboniferous magmatism in the west Junggar, Xinjiang: Implications for ridge subduction? Chem. Geol. 266 (3–4), 364–389. https://doi.org/10.1016/j.chemgeo.2009.07.001.

Guy, A., Schulmann, K., Soejono, I., Xiao, W., 2020. Revision of the Chinese Altai-East Junggar terrane accretion model based on geophysical and geological constraints. Tectonics 39, e2019TC006026. https://doi.org/ 10.1029/2019TC006026.

He, R., Gao, R., Li, Q., Guan, Y., Li, P., 2001. Corridor gravity fields and crustal density structures in Tianshan (Dushanzi)-West Kunlun (quanshuigou) GGT. Acta Geosci. Sin. 22 (6), 553–558 in Chinese with English abstract.

Hu, A., Zhang, G., Chen, Y., Zhang, Q., 2001. A model of division of the continental crust basement and the time scales of the major geological events in the xinjiang-based on studies of isotopic geochronology and geochemistry. Xingjiang Geology 19 (1), 12–19 in Chinese with English abstract.

Jahn, B.M., Wu, F., Chen, B., 2000. Granitoids of the Central Asian Orogenic Belt and continental growth in the Phanerozoic. Trans. R Soc. Edinb. Earth Sci. 91, 181–193.

Jiang, Y., 1984. A Preliminary approach to the basement of Junggar district. Xingjiang Geol. 2 (1), 11–16 in Chinese with English abstract.

Jiang, Y., Schulmann, K., Sun, M., Štípská, P., Guy, A., Janoušek, V., Lexa, O., Yuan, C., 2016. Anatexis of accretionary wedge, Pacific-type magmatism, and formation of vertically stratified continental crust in the Altai Orogenic Belt. Tectonics 35, 3095-3118. https://doi.org/ 10.1002/2016TC004271.

Jiang, J., Štípská, P., Sun, M., Schulmann, K., Zhang, J., Wu, Q., Long, X., Yuan, C., Pacek, M., Zhang, G., Xiao, W., 2015. Juxtaposition of Barrovian and migmatite domains in the Chinese Altai: a result of crustal thickening followed by doming of partially molten lower crust. J. Metamorphic Geol. 33, 45–70.

Jiang, Y., Štípská, P., Schulmann, K., Aguilar, C., Wang, S., Anczkiewicz, R., Zhang, J., Li, P., Chopin, F., 2021. Barrovian and Buchan metamorphic series in the Chinese Altai P-T-t-D evolution and tectonic implications. J. Metamorphic Geol. 40, 823–857.

Kong, L., Jiang, Y., Schulmann, K., Zhang, J., Weinberg, R.F., Sun, M., Wang, S., Shu, T., Ning, J., 2022. Petrostructural and geochronological constraints on Devonian extension-shortening cycle in the Chinese Altai: Implications for retreating-advancing subduction. e2021TC007195 Tectonics 41. https://doi.org/10.1029/2021TC007195.

Laske, G., Ma, Z., Masters, G., Pasyanos, M., 2021. A new global crustal model at 1x1 degree (Crust 1.0). https://igppweb.ucsd.edu/~gabi/crust1.html.

Li, C., 1985. Discussion on the division of continental paleoplates. China Geol. 1, 13–16 in Chinese.

Li, C., 1986. On Terrane. Geol. Rev. 32 (6), 578–582 in Chinese with English abstract.

Li, D., He, D., Tang, Y., 2016. Reconstructing multiple arc-basin systems in the Altai–Junggar area (NW China): Implications for the architecture and evolution of the western Central Asian Orogenic Belt. J. Asian Earth Sci. 121, 84–107. https://doi.org/10.1016/j.jseaes.2016.02.010.

Li, C., Wang, S., Wang, L., 2019. Tectonostratigraphic history of the southern Tian Shan, western China, from seismic reflection profile. J. Asian Earth Sci. 172, 101–114.

Li, J., Xiao, X., Tang, Y., Zhao, M., Feng, Y., Zhu, B., 1988. New progress in the study of paleoplate tectonics in the Karamaili region of East Junggar, Xinjiang. Chin. Sci. Bull. 10, 762–764 in Chinese.

Li, J., He, G., Xu, X., Li, H., Sun, G., Yang, T., Gao, L., Zhu, Z., 2006. Crustal tectonic framework of northern Xinjiang and adjacent regions and its formation. Acta Geol. Sin. 80, 149–168 in Chinese with English abstract.

Li, Z., Huang, B., Xiao, W., Yang, L., Qiao, Q., 2015. Paleomagnetic study of Late Paleozoic rocks in the Tacheng Basin of West Junggar (NW China): Implications for the tectonic evolution of the Western Altaids. Gondw. Res. 27, 862–877.

Li, Y., Oldenburg, D.W., 1996. 3-D inversion of magnetic data. Geophysics 61, 394–408.

Li, Y., Oldenburg, D.W., 2000. Joint inversion of surface and three-component borehole magnetic data. Geophysics 65, 540–552.

Li, Y., Liu, Q., Cheng, J., Li, S., Guo, B., Nai, Y., 2007. Crust and upper mantle shear velocity structure beneath Tian Shan. Sci. China (D: Earth Sciences) 37 (1), 1–9 in Chinese with English abstract.

Li, L., Xiao, W., Windley, B.F., Mao, Q., Jia, X., Yang, H., Tan, Z., Sang, M., Gan, J., Abuduxun, J., 2021. Contrasting Early Palaeozoic provenance of the Yemaquan and Harlik arcs in the SW Altaids (NW China): identification of cryptic sutures in accretionary orogens. Int. Geol. Rev. 63 (17), 2192–2214.

Liang, Y., Zhang, K., Li, W., 1999. Preliminary discussion of the crustal structure of Junggar orogenic belt. Xinjiang Geol. 17 (4), 305–311 in Chinese with English abstract.

Long, X., Yuan, C., Sun, M., Xiao, W., Zhao, G., Wang, Y., Cai, K., Xia, X., Xie, L., 2010a. Detrital zircon U-Pb ages and Hf isotopes of the early Paleozoic flysch sequence in the Chinese Altai, NW China: new constrains on depositional age, provenance and tectonic evolution. Tectonophysics 480, 213–231.

Long, X., Yuan, C., Sun, M., Zhao, G., Xiao, W., Wang, Y., Yang, Y., Hu, A., 2010b. Archean crustal evolution of the northern Tarim craton, NW China: Zircon U-Pb and Hf isotopic constraints. Precambr. Res. 180 (3), 272–284.

Long, X., Yuan, C., Sun, M., Xiao, W., Zhao, G., Zhou, K., Wang, Y., Hu, A., 2011. The discovery of the oldest rocks in the Kuluketage area and its geological implications. Science China (Earth Sciences) 54 (3), 342–348.

Lu, D., Li, Q, Gao, R., Li, Y., Li, D., Liu, W., Zhang, Z., 2000. Artificial explosion seismic profile across the Tianshan Mountains. Scientia Sinica (Terrae), S1, 45(9), 16-21 (in Chinese).

Lu, S., Li, H., Zhang, C., Niu, G., 2008. Geological and geochronological evidence for the Precambrian evolution of the Tarim Craton and surrounding continental fragments. Precambr. Res. 160 (1–2), 94–107.

Ma, G., Meng, Q., Wang, T., 2019. Deep dynamics analysis in Northeast China based on features of gravity data. Chin. J. Geophys. 62 (3), 1083–1092 in Chinese with English abstract.

Ma, X., Shu, L., Meert, J.G., Li, J., 2014. The Paleozoic evolution of Central Tianshan: Geochemical and geochronological evidence. Gondw. Res. 25, 797–819.

Mao, Q., Xiao, W., Fang, T., Wang, J., Han, C., Sun, M., Yuan, C., 2012. Late Ordovician to early Devonian adakites and Nb-enriched basalts in the Liuyuan area, Beishan, NW China: Implications for early Paleozoic slab–melting and crustal growth in the southern Altaids. Gondw. Res. 22, 534–553.

Mao, Q., Ao, S., Windley, B.F., Zhang, Z., Sang, M., Tan, Z., Wang, H., Li, R., Xiao, W., Pan, Z., 2022. Middle-Late Triassic southward–younging granitoids: Tectonic transition from subduction to collision in the Eastern Tianshan-Beishan Orogen, NW China. GSA Bull. 134 (9–10), 2206–2224. https://doi.org/10.1130/B36172.1.

Molnar, P., Tapponnier, P., 1975. Cenozoic tectonics of Asia: effects of continental collision. Science 189, 419–426.

Qiu, D., 1989. Analysis of the Carboniferous sedimentary basins in northwest China. Lithofacies Palaeogeogr. 42, 1–12 in Chinese with English abstract.

Qu, G., Li, Y., Chen, J., Ning, B., Li, Y., Li, J., Yin, J., 2003. Geometry, kinematics and tectonic evolution of Kepingtagh thrust system. Earth Sci. Front. 10 (S1), 142–152 in Chinese with English abstract.

Ren, J., 1984. The Indosinian orogeny and its significance in the tectonic evolution of China. Bull. Chin. Acad. Geol. Sci. 9, 31–44 in Chinese with English abstract.

Ren, J., 2015. International geological map of Asia (1:5,000,000). Geological Publishing House, Beijing.

Şengör, A.M.C., Natal'in, B.A., 1996. Turkic-type orogeny and its role in the making of the continental crust. Annu. Rev. Earth Planet Sci. 24, 263–337.

Şengör, A.M.C., Sunal, G., Natal'in, B.A., van der Voo, R., 2022. The Altaids: A review of twenty-five years of knowledge accumulation. Earth Science Reviews 228, 104013.

Song, P., Wang, T., Tong, Y., Zhang, J., Huang, H., Qin, Q., 2019. Contrasting deep crustal compositions between the Altai and East Junggar orogens, SW Central Asian Orogenic Belt: Evidence from zircon Hf isotopic mapping. Lithos 328–329, 297–311.

Su, Y., Tang, H., Hou, G., Liu, C., 2006. Geochemistry of aluminous A-type granites along Darabut tectonic belt in west Junggar, Xinjiang. Geochemistry 35, 55–67 in Chinese with English abstract.

Sun, M., Yuan, C., Xiao, W., Long, X., Xia, X., Zhao, G., Lin, S., Wu, F., Kröner, A., 2008. Zircon U-Pb and Hf isotopic study of gneissic rocks from the Chinese Altai: progressive accretionary history in the early to middle Palaeozoic. Chem. Geol. 247, 352–383.

Tapponnier, P., Molnar, P., 1979. Active faulting and Cenozoic tectonics of the Tien Shan, Mongolia, and baykal regions. J. Geophys. Res.-Solid Earth 84, 3425–3459.

Tian, W., Campbell, I.H., Allen, C.M., Guan, P., Pan, W., Chen, M., Yu, H., Zhu, W., 2010. The Tarim picrite-basalt-rhyolite suite, a Permian flood basalt from northwest China with contrasting rhyolites produced by fractional crystallization and anatexis. Contrib. Miner. Petrol. 160 (3), 407–425. https://doi.org/10.1007/s00410-009-0485-3.

Tian, Z., Xiao, W., Windley, B.F., Huang, P., Zhang, J., Ao, S., Zhang, Z., Song, D., Liu, F., 2021. Two key switches in regional stress field during multi-stage deformation in the Carboniferous–Triassic southernmost Altaids (Beishan, NW China): Response to orocline-related roll-back processes. GSA Bull. (11/12), 133.

Tikhonov, A.N., Arsenin, V.Y., 1977. Solutions of Ill-posed Problems. Washington DC: V. H. Wiston and Sons.

Turner, S.A., Cosgrove, J.W., Liu, J., 2010. Controls on lateral structural variability along the Keping Shan thrust belt, SW Tien Shan foreland, China. Geol. Soc. 348, 71–85. https://doi.org/10.1144/SP348.5.

Wang, H., 1986. Precambrian geochronologic and chronostratigraphic subdivision of China. Earth Sci.-J. Wuhan College Geol. 11 (5), 447–453 in Chinese with English abstract.

Wang, Y., Han, G., Jiang, M., Yuan, X., 2004. Crustal structure along the geosciences transect from Altay to Altun Tagh. Chin. J. Geophys. 47 (2), 240–249 in Chinese with English abstract.

Wang, T., Hong, D., Jahn, B.M., Tong, Y., Wang, Y., Han, B., Wang, X., 2006. Timing, petrogenesis, and setting of Paleozoic synorogenic intrusions from the Altai Mountains, northwest China: Implications for the tectonic evolution of an accretionary orogen. J. Geol. 114 (6), 735–751.

Wang, T., Jahn, B.M., Kovach, V.P., Tong, Y., Hong, D., Han, B., 2009. Nd–Sr isotopic mapping of the Chinese Altai and implications for continental growth in the Central Asian Orogenic Belt. Lithos 110, 359–372.

Wang, T., Tong, Y., Zhang, L., Li, S., Huang, H., Zhang, J., Guo, L., Yang, Q., Hong, D., Donskaya, T., Gladkochub, D., Tserendash, N., 2017. Phanerozoic granitoids in the central and eastern parts of Central Asia and their tectonic significance. J. Asian Earth Sci. 145 (B), 368–392. https://doi.org/10.1016/j.jseaes.2017.06.029.

Wang, T., Huang, H., Song, P., Wu, H., Zhang, J., Tong, Y., Du, K., Qin, Q., 2020. Studies of crustal growth and deep lithospheric architecture and new issues: exemplified by the Central Asian Orogenic Belt (Northern Xinjiang). Earth Sci. 45 (7), 2326–2344 in Chinese with English abstract.

Wang, T., Tong, Y., Huang, H., Zhang, H., Guo, L., Li, Z., Wang, X., Eglington, B., Li, S., Zhang, J., Donskaya, T.V., Petrov, O., Zhang, L., Song, P., Zhang, X., Wang, C., 2023a. Granitic record of the assembly of the Asian continent. Earth Sci. Rev. 237, 104298.

Wang, T., Huang, H., Zhang, J., Wang, C., Cao, G., Xiao, W., Yang, Q., Bao, X., 2023b. Voluminous continental growth of the Altaids and its control on metallogeny. Natl. Sci. Rev. 10 (2), nwac283.

Wang, S., Jiang, Y., Weinberg, R., Schulmann, K., Zhang, J., Li, P., Xiao, M., Xia, X., 2021. Flow of Devonian anatectic crust in the accretionary Altai Orogenic Belt, central Asia: Insights into horizontal and vertical magma transfer. GSA Bull. 133 (11/12), 2501–2523.

Wang, W., Zhang, G., Liang, J., 2010. Spatial variation law of vertical derivative zero points for potential field data. Applied Geophysic 7 (3), 197–209.

Wei, C., Clarke, G., Tian, W., Qiu, L., 2007. Transition of metamorphic series from the Kyanite- to andalusite-types in the Altai orogen, Xinjiang, China: Evidence from petrography and calculated KMnFMASH and KFMASH phase relations. Lithos 96, 353–374.

Wilhem, C., Windley, B.F., Stampfli, G.M., 2012. The Altaids of Central Asia: A tectonic and evolutionary innovative review. Earth Sci. Rev. 113, 303–341. https://doi.org/10.1016/j.earscirev.2012.04.001.

Windley, B.F., Allen, M.B., Zhang, C., Zhao, Z., Wang, G., 1990. Paleozoic accretion and Cenozoic redeformation of the Chinese Tien Shan range, central Asia. Geology 18, 128–131.

Windley, B.F., Alexeiev, D., Xiao, W., Kröner, A., Badarch, G., 2007. Tectonic models for accretion of the Central Asian orogenic belt. Journal of the Geological Society 164, 31–47.

Wu, Q., 1986. Structural evolution and prospects of Junggar Basin. Xinjiang Geol. 4 (3), 1–10 in Chinese with English abstract.

Wu, B., He, G., Wu, T., Li, H., Luo, H., 2006. Discovery of the Buergen ophiolitic mélange belt in Xinjiang and its tectonic significance. Geol. China 33 (3), 476–486 in Chinese with English abstract.

Wu, S., Huang, R., Xu, Y., Yang, Y., Jiang, X., Zhu, L., 2018. Seismological evidence for a remnant oceanic slab in the western Junggar, Northwest China. J. Geophys. Res. Solid Earth 123, 4157–4170. https://doi.org/10.1029/2017JB015332.

Wu, G., Li, H., Xu, Y., Su, W., Chen, Z., Zhang, B., 2012. The tectonothermal events, architecture and evolution of Tarim craton basement palaeo-uplifts. Acta Petrol. Sin. 28 (8), 2435–2452 in Chinese with English abstract.

Xiao, W., Han, C., Yuan, C., Sun, M., Lin, S., Chen, H., Li, Z., Li, J., Sun, S., 2008. Middle Cambrian to Permian subduction–related accretionary orogenesis of northern Xinjiang, NW China: Implications for the tectonic evolution of Central Asia. J. Asian Earth Sci. 32 (2–4), 102–117. https://doi.org/10.1016/j.jseaes.2007.10.008.

Xiao, W., Huang, B., Han, C., Sun, S., Li, J., 2010. A review of the western part of the Altaids: A key to understanding the architecture of accretionary orogens. Gondw. Res. 18, 253–273.

Xiao, W., Santosh, M., 2014. The western Central Asian Orogenic Belt: A window to accretionary orogenesis and continental growth. Gondw. Res. 25, 1429–1444.

Xiao, W., Shu, L., Gao, J., Xiong, X., Wang, J., Guo, Z., Li, J., Sun, M., 2009. Continental dynamics and mineralization in the Central Asian Orogenic Belt. Basic Sci. China-Res. Progr. 14–19 in Chinese with English abstract.

Xiao, X., Tang, Y., Wang, J., Gao, J., Zhao, M., 1994. Bluechist belts and their tectonic implications of the S. Tianshan Mts., N.W. China. Acta Geoscientia Sinica 3–4, 54–64 in Chinese with English abstract.

Xiao, W., Windley, B.F., Mark, B., Allen, M., Han, C., 2013. Paleozoic multiple accretionary and collisional tectonics of the Chinese Tianshan orogenic collage. Gondw. Res. 23, 1316–1341.

Xiao, W., Kusky, T., Safonova, I., Seltmann, R., Sun, M., 2015a. Tectonics of the Central Asian Orogenic Belt and its Pacific analogues. J. Asian Earth Sci. 113 (1), 1–6. https://doi.org/10.1016/j.jseaes.2015.06.032.

Xiao, W., Windley, B.F., Sun, S., Li, J., Huang, B., Han, C., Yuan, C., Sun, M., Chen, H., 2015b. A Tale of Amalgamation of Three Permo-Triassic Collage Systems in Central Asia: Oroclines, Sutures, and Terminal Accretion. Annu. Rev. Earth Planet. Sci. 43, 477–507.

Xiao, W., Windley, B.F., Han, C., Liu, W., Wan, B., Zhang, J., Ao, S., Zhang, Z., Song, D., 2018. Late Paleozoic to early Triassic multiple roll-back and oroclinal bending of the Mongolia collage in Central Asia. Earth Sci. Rev. 186, 94–128.

Xiao, W., Song, D., Windley, B., Li, J., Han, C., Wan, B., Zhang, J., Ao, S., Zhang, Z., 2019. Research progresses of the accretionary processes and metallogenesis of the Central Asian Orogenic Belt. Sci. China Earth Sci. 49, 1512–1545 in Chinese with English abstract.

Xu, S., Chen, C., Du, J., Sun, S., Hu, Z., 2015. Characteristics and tectonic implications of lithospheric density structures beneath western Junggar and its surroundings. Earth Sci.-J. China Univ. Geosci. 40 (9), 1556–1565 in Chinese with English abstract.

Xu, M., Wang, L., Zhong, K., Hu, D., Li, H., Hu, X., 2005. Features of gravitational and magnetic fields in the Tarim Basin and basement structure analysis. Geol. J. China Univ. 11 (4), 585–592 in Chinese with English abstract.

Xu, X., Wang, H., Li, P., Chen, J., Ma, Z., Zhu, T., Wang, N., Dong, Y., 2013. Geochemistry and geochronology of Paleozoic intrusions in the Nalati (Narati) area in western Tianshan, Xinjiang, China: Implications for Paleozoic tectonic evolution. J. Asian Earth Sci. 72, 33–62. https://doi.org/10.1016/j.jseaes.2012.11.023.

Xu, Y., Yang, B., Zhang, S., Liu, Y., Zhu, L., Huang, R., Chen, C., Li, Y., Luo, Y., 2016. Magnetotelluric imaging of a fossil paleozoic intraoceanic subduction zone in western Junggar, NW China. J. Geophys. Res. Solid Earth 121, 4103–4117. https://doi.org/10.1002/2015JB012394.

Xu, Y., Yang, B., Zhang, A., Wu, S., Zhu, L., Yang, Y., Wang, Q., Xia, Q., 2020. Magnetotelluric imaging of a fossil oceanic plate in northwestern Xinjiang, China. Geology 48, 385–389. https://doi.org/10.1130/G47053.1.

Yang, S., Chen, H., Li, Z., Li, Y., Yu, X., Li, D., Meng, L., 2013. Early Permian Tarim Large Igneous Province in northwest China. Sci. China Earth Sci. 56 (12), 2015–2026. https://doi.org/10.1007/s11430-013-4653-y.

Yang, G., Li, Y., Gu, P., Yang, B., Tong, L., Zhang, H., 2012. Geochronological and geochemical study of the Darbut Ophiolitic Complex in the west Junggar (NW China): Implications for petrogenesis and tectonic evolution. Gondw. Res. 21 (4), 1037–1049. https://doi.org/10.1016/j.gr.2011.07.029.

Yang, X., Xu, X., Qian, Y., Chen, Q., Chu, C., Jiang, H., 2014. Discussion on regional differences of basement composition of the Tarim Basin, NW China. Geotectonica et Metallogenia 38 (3), 544–556 in Chinese with English abstract.

Yang, X., Tian, X., Windley, B.F., Zhao, L., Lu, Y., Yuan, H., Xiao, W., 2022. The role of multiple trapped oceanic basins in continental growth: seismic evidence from the southern Altaids. Geophys. Res. Lett. 49 e2022GL098548.

Yang, W., Zhang, L., Xu, Y., Yu, C., Yu, P., Zhang, B., Yang, B., 2015a. Three dimensional electrical resistivity structures of the Tarim Basin. Acta Geological Sinica 89 (12), 2203–2212 in Chinese with English abstract.

Yang, W., Zhang, L., Xu, Y., Yu, C., Yu, P., Zhang, B., Yang, B., 2015b. Magnetotellruic investigation and 3D lithospheric structures in the Tarim terrane. Acta Geological Sinica 89 (7), 1151–1161 in Chinese with English abstract.

Ye, L., Zhang, D., Wang, S., Zhou, T., Yuan, F., White, N.C., Xiao, W., 2022. Genesis of Re-rich Molybdenite in the Baishan Mo deposit, Eastern Tianshan, Xinjiang, Northwest China. Resour. Geol. 72, e12269.

Yin, X., Li, Y., Liu, Z., 1998. Gravity field and crust-upper mantle structure over the Tarim Basin. Seismol. Geol. 20 (4), 370–378 in Chinese with English abstract.

Zhang, C., Li, H., Santosh, M., Li, Z., Zou, H., Wang, H., Ye, H., 2012. Precambrian evolution and cratonization of the Tarim Block, NW China: Petrology, geochemistry, Nd-isotopes and U-Pb zircon geochronology from Archaean gabbro-TTG-potassic granite suite and Paleoproterozoic metamorphic belt. J. Asian Earth Sci. 47, 5–20. https://doi.org/10.1016/j.jseaes.2011.05.018.

Zhang, J., Sun, M., Schulmann, K., Zhao, G., Wu, Q., Jiang, Y., Guy, A., Wang, Y., 2015. Distinct deformational history of two contrasting tectonic domains in the Chinese Altai_ Their significance in understanding accretionary orogenic process. J. Struct. Geol. 73, 64–82.

Zhang, J., Wang, T., Tong, Y., Zhou, Z., 2017. Tracking deep ancient crustal components by xenocrystic/inherited zircons of Palaeozoic felsic igneous rocks from the Altai-East Junggar terrane and adjacent regions, western Central Asian Orogenic Belt and its tectonic significance. Int. Geol. Rev. 59, 2021–2040.

Zhang, J., Chen, Y., Xiao, W., Wakabayashi, J., Windley, B.F., Yin, J., 2021. Sub-parallel ridge-trench interaction and an alternative model for the Silurian-Devonian archipelago in estern Junggar and North-Central Tiansh an in NW China. Earth Sci. Rev. 217, 103648.

Zhao, J., Li, Z., Cheng, H., Yao, C., Li, Y., 2004. Structure of lithospheric density and geomagnetism beneath the Tianshan orogenic belt and their geodynamic implications. Chin. J. Geophys. 47 (6), 1061–1067 in Chinese with English abstract.

Zhdanov, M.S., 2002. Geophyscal inverse theory and regularization problems. Elsevier Science, NewYork.

Zheng, Q., Xu, X., Zhang, W., Zheng, Y., Liu, Y., Kuang, X., Zhou, D., Yu, X., Wang, B., 2021. A fossil Paleozoic subduction-dominated tranch-arc-basin system revealed by airborne magnetic-gravity imaging in West Junggar, NW China. Front. Earth Sci. 9, 760305.

Zhu, X., Lu, M., 2016. Regional metallogenic structure based on aeromagnetic data in northern Chile. Appl. Geophys. 13 (4), 721–735.

Zhu, X., Lu, M., 2021. Fault structures and magmatic intrusions inferred from magnetic data for the Southern Great Xing'an Range, Northern China. Ore Geol. Rev. 135, 104206.

Zhu, X., Lu, M., Guan, Y., Zhang, Y., 2018. Experiment on revealing the regional metallogenic structure based on the aeromagnetic data in the southern Da Hinggan Mountains. Geol. China 37 (2/3), 299–313 in Chinese with English abstract.

Zhu, X., Zheng, H., Lu, M., 2019. Lateral variation of aeromagnetic anomaly in South China and its tectonic implications. Int. J. Earth Sci. 108 (5), 1493–1507.

Zhu, X., Wang, T., Huang, H., Zheng, H., 2022a. An aeromagnetic study of fault structures underneath the region across the Chinese Altai orogen, Junggar Basin, Tianshan orogen, and Tarim Basin. J. Asian Earth Sci. 239, 105418 https://doi.org/10.1016/j.jseaes.2022.105418.

Zhu, X., Lu, M., Zheng, H., 2022b. Bouguer gravity anomaly in the Andean orogenic belt and its dynamic implications for regional tectonic evolution. Acta Geologica Sinica – English Edition 96 (3), 806–824. https://doi.org/10.1111/1755-6724.14887.

Zhu, X., Wang, L., Zhou, X., 2022c. Structural features of the Jiangshao Fault Zone inferred from aeromagnetic data for South China and the East China Sea. Tectonophysics 826, 229252. https://doi.org/10.1016/j.tecto.2022.229252.

Zhu, W., Zheng, B., Shu, L., Ma, D., Wu, H., Li, Y., Huang, W., Yu, J., 2011. Neoproterozoic tectonic evolution of the Precambrian Aksu blueschist terrane, northwestern Tarim, China: Insights from LA-ICP-MS zircon U-Pb ages and geochemical data. Precambr. Res. 185 (3–4), 215–230. https://doi.org/10.1016/j.precamres.2011.01.012.